Low-lying dipole strength in ^{52}Cr

T. Shizuma,[1] T. Hayakawa,[1] I. Daito,[2] H. Ohgaki,[2] S. Miyamoto,[3] and F. Minato[4]

[1]*National Institutes for Quantum and Radiological Science and Technology, Tokai, Ibaraki 319-1106, Japan*
[2]*Institute of Advanced Energy, Kyoto University, Uji, Kyoto 611-0011, Japan*
[3]*Laboratory of Advanced Science and Technology for Industry, University of Hyogo, Kamigori, Hyogo 678-1205, Japan*
[4]*Japan Atomic Energy Agency, Tokai, Ibaraki 319-1195, Japan*

The low-lying dipole strength in ^{52}Cr was measured in nuclear resonance fluorescence experiments using a quasimonochromatic, linearly polarized photon beam. The parities of the excited dipole states were determined by the intensity asymmetry of resonantly scattered γ rays with respect to the polarization plane of the incident photon beam. We observed 62 resonances at excitation energies between 7.5 and 12.1 MeV. The observed $M1$ and $E1$ strengths were compared via random-phase-approximation calculations using the Skyrme interaction. The effects of two-particle–two-hole configuration mixing and tensor force on dipole strength distributions were investigated.

I. INTRODUCTION

Low-lying electric ($E1$) and magnetic ($M1$) dipole excitations are fundamental excitation modes in atomic nuclei [1,2]. The observation of $E1$ and $M1$ states provides information on various collective and single-particle motions related to the nuclear dipole resonances, such as the spin-flip $M1$ resonance and the $E1$ pygmy dipole resonance (PDR).

Nuclei in the vicinity of the closed $N = Z = 28$ shells represent one of the most favorable regions for observing spin-flip $M1$ resonance. In these nuclei, a strong spin-flip $M1$ transition occurs because of proton and neutron $1f_{5/2} \otimes 1f_{7/2}^{-1}$ particle-hole excitation [3]. The ^{52}Cr nucleus lies in this region and differs from the doubly magic ^{56}Ni nucleus by four nucleons because it has four fewer protons, that is, $\pi 1 f_{7/2}^{-4}$ to the ^{56}Ni core. In previous inelastic electron scattering measurements [4–7], the $M1$ strength associated with this particle-hole excitation was observed at excitation energies between 7 and 10 MeV. The observed excitation energy can be connected to the repulsive nature of the residual interaction relevant to the isovector $M1$ excitation. The $M1$ strength distribution is also affected by core polarization, two-particle–two-hole (2p2h) configuration mixing, and tensor force [8–10].

The concentration of the $E1$ strength around the particle separation energy is commonly referred to as PDR because the strength is weak relative to that of the giant dipole resonance (GDR), which is the dominant part of the $E1$ strength in nuclei. Such a concentration has been observed experimentally in several stable and unstable nuclei [11–17]. The PDR strength is correlated with neutron skin thickness [18], which is related to the equation of state (EOS) of the neutron-rich matter [19] and may provide information on the properties of neutron stars, such as the proton ratio and radius. The total sum of the measured energy-weighted strengths of such $E1$ concentrations is less than 1% of the Thomas-Reiche-Kuhn (TRK) sum rule value for stable nuclei and less than 5% for unstable neutron-rich nuclei. For stable pf-shell nuclei, a relatively small low-energy $E1$ strength, $\approx 0.3\%$ of the TRK sum rule value, was observed below 10 MeV in ^{56}Fe and ^{58}Ni [20,21]. However, little detailed information on this low-energy $E1$ excitation is available in other pf-shell nuclei.

In nuclear resonance fluorescence (NRF) measurements, transition strength can be extracted from the measured scattering intensities in a model-independent fashion [22], as the NRF occurs only via electromagnetic interactions. It has been shown that a quasimonochromatic, linearly polarized photon beam produced by laser Compton scattering (LCS) considerably increases experimental sensitivities, particularly for the determination of the parity quantum numbers of resonantly excited states [23,24]. Information on the dipole excitations in ^{52}Cr has been obtained from several NRF experiments using unpolarized or partially polarized bremsstrahlung [25–29]. A recent investigation [30] also provided the parity assignment to the dipole states at excitation energies between 5 and 9.5 MeV using a linearly polarized photon beam. However, above 9.5 MeV, the information on dipole states in ^{52}Cr is scarce.

In the present work, NRF measurements on ^{52}Cr were performed using a quasimonochromatic, linearly polarized photon beam to investigate the low-lying $E1$ and $M1$ states up to excitation energies close to the neutron separation energy ($S_n = 12.039$ MeV). The results are compared with those obtained via random-phase-approximation (RPA) calculations using the Skyrme interaction [31].

II. EXPERIMENTAL PROCEDURE

The present NRF measurements were performed at the NewSUBARU synchrotron radiation facility at the University of Hyogo [32,33]. A quasimonochromatic, linearly polarized photon beam was generated by LCS between laser light and electrons circulating a storage ring. A Nd:YVO$_4$ laser with a wavelength of 1064 nm operated at a frequency of 20 kHz was used. The electron energies were selected as 683, 708, 731, 756, 792, and 828 MeV to produce quasimonochromatic photon beams with maximum energies $E_\gamma^{\max}$ of 8.2, 8.8, 9.4, 10.1, 11.0, and 12.1 MeV, respectively. A lead collimator with

a 10-cm thickness and 3-mm aperture was used to form a quasimonochromatic photon beam with an energy spread of $\Delta E/E \approx 3$ to 5% at full width at half maximum (FWHM). The photon flux was measured during the NRF measurement at each LCS photon energy by a large volume ($8'' \times 12''$) NaI(Tl) scintillation detector. The average intensity on the target was 6×10^5 photons per second. The target consisted of a natural chromium cylinder (the isotopic abundance of ^{52}Cr is 83.789%) 10 mm in diameter and 30 mm long. Two high-purity germanium (HPGe) detectors with efficiencies of 120% and 140% relative to a $3'' \times 3''$ NaI scintillation detector were used to measure scattered photons from the target. These detectors were placed in vertical and horizontal planes at a scattering angle of $\theta = 90°$. The typical energy resolution of the HPGe detectors was $\Delta E_\gamma/E_\gamma \approx 0.09\%$ at $E_\gamma \approx 7$ MeV. To reduce the background counts originating from bremsstrahlung because of high-energy electrons in the storage ring, events within 1 μs of laser pulses were stored in a list mode. The γ-ray energies were calibrated using the known γ-ray peaks at 6740.8, 7896.8, 9139.4, 9211.0, and 9235.7 keV in ^{52}Cr taken from Ref. [29]. We calculated the relative efficiencies for the HPGe detectors using Electron Gamma Shower (EGS5) [34]. The calculated efficiency curves were verified using efficiencies obtained from measurements with a ^{152}Eu standard source and resonances of ^{208}Pb.

Figure 1 presents a typical energy spectrum for the incident photon beam at $E_\gamma^{\max} = 9.4$ measured by a $3.5'' \times 4''$ LaBr$_3$(Ce) scintillation detector. A Monte Carlo simulation was performed with the EGS5 code to analyze the response of the LaBr$_3$(Ce) scintillation detector. The energy distribution of the incident photon beam was extracted by unfolding the resulting simulated spectrum so as to reproduce the observed energy distribution as shown in Fig. 1.

The intensity asymmetry of the resonantly scattered photons with respect to the polarization plane of the incident pho-
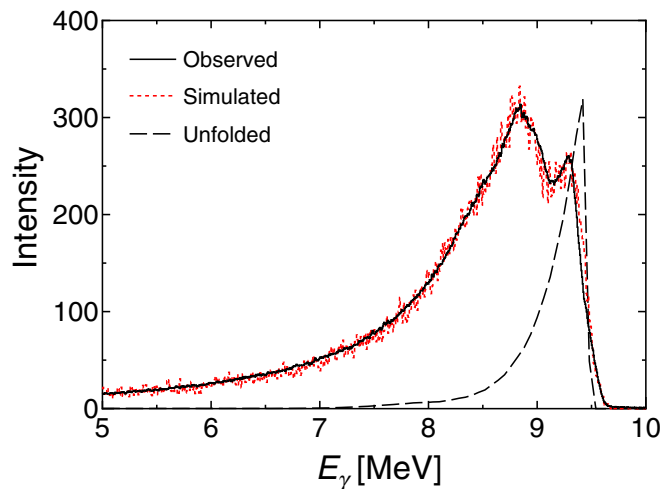
ton beam can be used for parity determination. The azimuthal angular distribution of dipole transitions is expressed as

$$W(\theta,\phi) = W(\theta) \mp \tfrac{3}{4}(1-\cos^2\theta)\cos2\phi, \qquad (1)$$

where θ is the scattering angle of photons with respect to the incoming photon beam and ϕ is the azimuthal angle between the polarization plane (formed by the propagation direction and the electric field vector of the incident photon beam) and the reaction plane. $W(\theta)$ is the angular correlation function for unpolarized dipole radiation. Here, the minus (plus) sign corresponds to $E1$ ($M1$) transitions. A more general form of Eq. (1) can be found in Ref. [35].

The analyzing power is defined in Ref. [23] using the azimuthal angular distributions at $\phi = 0°$ and 90° as

$$\Sigma = \frac{W(90°,0°) - W(90°,90°)}{W(90°,0°) + W(90°,90°)}. \qquad (2)$$

Under the condition of complete polarization of the incoming photon beam, $\Sigma = +1$ is expected for $M1$ transitions and $\Sigma = -1$ is expected for $E1$ transitions.

The corresponding intensity asymmetry of the observed NRF γ rays is given by

$$A = \frac{N_\parallel - N_\perp}{N_\parallel + N_\perp} = q\Sigma, \qquad (3)$$

where $N_\parallel$ ($N_\perp$) represents the measured intensity of NRF γ rays detected at $\theta = 90°$ in the plane parallel (perpendicular) to the polarization plane. Here, q is the experimental sensitivity, which is less than unity because of the finite solid angle of the HPGe detectors and the spatially extended target. In the present case, q is estimated to be 0.8 by the numerical simulation. Thus, based on the azimuthal intensity asymmetry, the multipolarity of resonantly scattered transitions can be determined.

III. RESULTS

Figures 2 and 3 present the photon-scattering spectra obtained at polar and azimuthal angles of $(\theta,\phi) = (90°,0°)$ and $(90°,90°)$. Peaks shown with spin and parity represent ground-state transitions. Here, the parities of the excited states were determined based on the azimuthal intensity asymmetry from Eqs. (2) and (3), as shown in Fig. 4. We observed a total of 62 resonances between 7.5 and 12.1 MeV.

The scattering strength Γ_0^2/Γ for an excited state at an energy of E_x can be deduced from the measured intensity of the respective transition [22]. Here, Γ and Γ_0 are the total radiative width and the decay width to the ground state, respectively. In the present analysis, $\Gamma_0^2/\Gamma(E_x)$ for a dipole state was deduced relative to the known $\Gamma_0^2/\Gamma(E_{x,\mathrm{ref}})$ for the 9139- and 9211-keV states in ^{52}Cr:

$$\frac{\Gamma_0^2/\Gamma(E_x)}{\Gamma_0^2/\Gamma(E_{x,\mathrm{ref}})} = \frac{I_\gamma E_\gamma^2}{\Phi \lambda} \frac{\Phi' \lambda'}{I_\gamma' E_\gamma'^2}. \qquad (4)$$

Here, I_γ and I_γ' denote the measured intensities of a transition at E_γ and of the reference transitions. Φ and Φ' represent

FIG. 1. Typical energy distribution of the incident photon beam at $E_\gamma^{\max} = 9.4$ MeV measured using a LaBr$_3$(Ce) scintillation detector (solid line). The original LCS photon spectrum, shown as the dashed line, was obtained by unfolding the simulated energy distribution (dotted line).
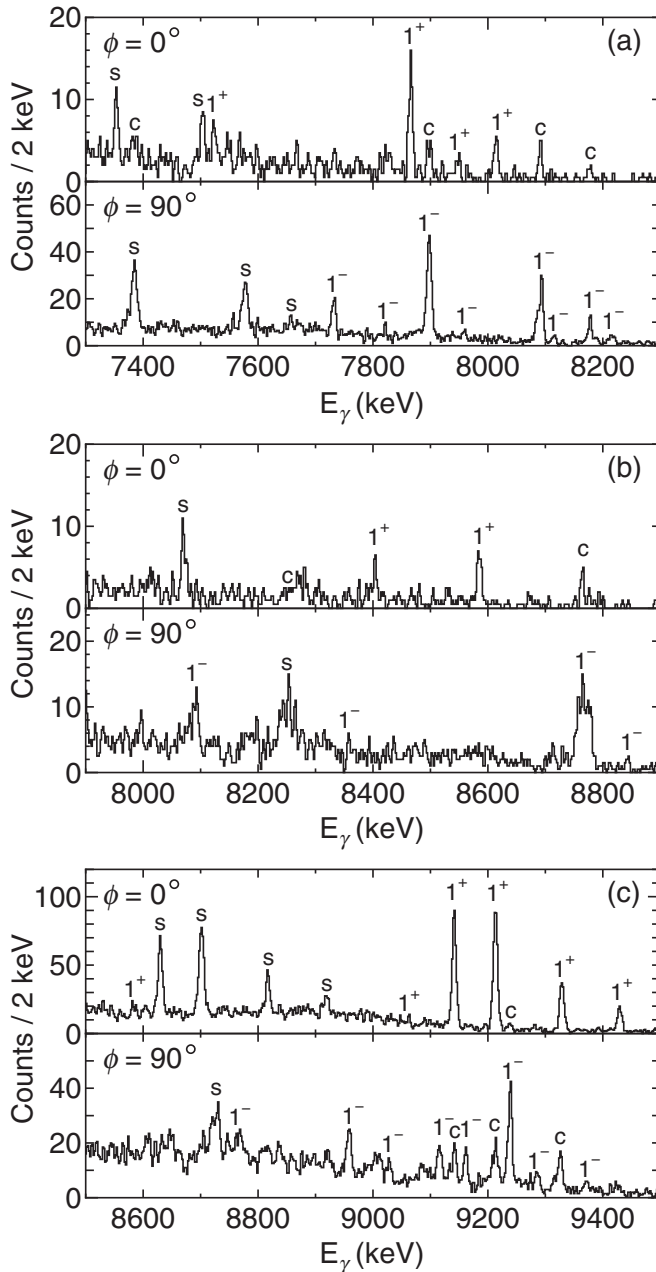
FIG. 2. Photon scattering spectra measured at polar and azimuthal angles of $(\theta,\phi) = (90°,0°)$ and $(90°,90°)$ using the photon beam with $E_\gamma^{\max}$ of (a) 8.2 MeV, (b) 8.8 MeV, and (c) 9.4 MeV, respectively. The J^π assignments are indicated for the ground-state transitions in ^{52}Cr. Peaks labeled c and s are attributable to contamination from the opposite-parity transitions and single escapes, respectively.

FIG. 3. Same as Fig. 2, but with $E_\gamma^{\max}$ of (a) 10.1, (b) 11.0, and (c) 12.1 MeV.

the photon fluxes at the energy of the considered level and the reference levels, respectively. λ and λ' are the correction factors of atomic and self-absorption for the level at E_x and for the reference level. Because the previous measurements [25,27,29] provide a consistent result for the scattering strength Γ_0^2/Γ of the resonance at 9139 keV, the 9139-keV transition was used as a reference. The correction factors λ and λ' were determined according to Eq. (19) in Ref. [36].
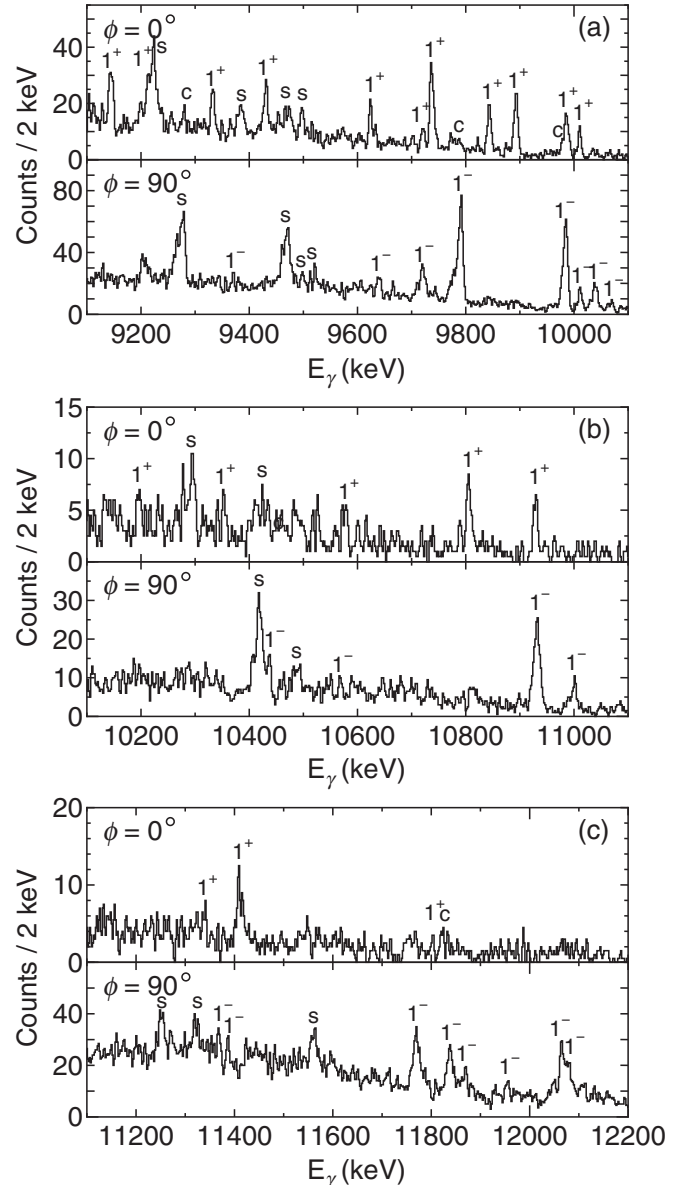
The reduced transition probability can be extracted from the ground-state decay width Γ_0 using the following relationships:

$$B(E1)\uparrow = 2.866\frac{\Gamma_0}{E_\gamma^3} \; [10^{-3}e^2\text{fm}^2], \qquad (5)$$

$$B(M1)\uparrow = 0.2598\frac{\Gamma_0}{E_\gamma^3} \; [\mu_N^2], \qquad (6)$$

where Γ_0 is given in units of meV and E_γ in units of MeV. The results are summarized in Tables I and II. Since in the present measurement the natural chromium was used, possibilities of influence of other stable chromium isotopes could not be excluded. Therefore, the resonances assigned to ^{52}Cr in previous NRF measurements [25–27,29] are listed in Table I. On the other hand, the resonances newly observed in this
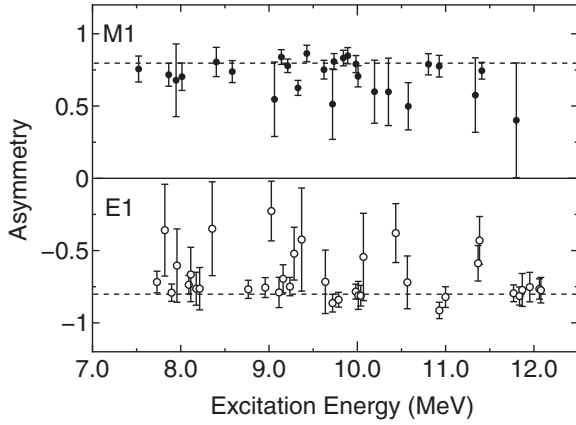
FIG. 4. Azimuthal intensity asymmetry obtained for $E1$ (open circles) and $M1$ (filled circles) transitions in ^{52}Cr. The experimental sensitivity $q(= 0.8)$ deduced from the numerical calculation is indicated by dashed lines.

work are listed in Table II as possible resonances in ^{52}Cr. In a previous measurement [37], 7948-, 9208-, and 9719-keV $M1$ transitions were observed in ^{50}Cr. Contributions of these transitions to the strengths of the 7947-, 9211-, and 9721-keV resonances were subtracted. Since no NRF data are available

for ^{53}Cr and ^{54}C, the present data may include contributions from these isotopes.

For the energy region from 7.5 to 12.1 MeV, we observed 26 positive-parity and 36 negative-parity states. The parity assignments for the known resonances, whose spin and parity are shown without parentheses in Table I, are consistent with the previous results [26,30]. We also confirmed six states at 9735.6, 9982.0, 10435, 10929, 11769, and 11836 keV, which were observed via previous NRF measurements [26]. In addition, we observed 18 positive-parity and 23 negative-parity states listed in Table II. For the positive-parity states, if the corresponding $M1$ resonances were observed in the ^{52}Cr(e, e') measurement [5], we assigned spin and parity of $(1)^+$ or (1^+) for these states. By contrast, for the negative-parity states, spin and parity of $(1)^-$ or (1^-) are preferred because higher multipole order transitions with negative-parity natures, such as $M2$ and $E3$, are unlikely to be observed in NRF experiments.

The scattering strengths of Γ_0^2/Γ based on previous measurements [25,27,29] are also listed in Table I. The values for 7730-, 7896-, 8014-, 8091-, 8175-, 8764-, 9139-, 9211-, and 9236-keV are consistent with the the previous NRF measurements [25,29].

In this work, the summed $M1$ strength at $E_x = 7.5$ to 12.1 MeV is determined to be $\Sigma B(M1)\uparrow = 4.25(32)\,\mu_N^2$, or if

TABLE I. Transition energies E_γ, intensity asymmetry A, spin and parity assignments J^π, scattering strengths Γ_0^2/Γ, and reduced transition probabilities $B(\sigma 1)\uparrow$ for the observed resonances in ^{52}Cr. Previously determined Γ_0^2/Γ values are also listed for comparison.

E_γ (keV)	A	J^π	$\Gamma_0^2/\Gamma^{\mathrm{a}}$ (eV)	$\Gamma_0^2/\Gamma^{\mathrm{b}}$ (eV)	$\Gamma_0^2/\Gamma^{\mathrm{c}}$ (eV)	$\Gamma_0^2/\Gamma^{\mathrm{d}}$ (eV)	$B(E1)\uparrow^{\mathrm{e}}$ $(10^{-3}\,e^2\,\mathrm{fm}^2)$	$B(M1)\uparrow^{\mathrm{e}}$ (μ_N^2)
7522.5(10)	0.76(9)	1^+	2.1(4)	0.400(28)	0.97(23)			1.3(2)
7730.3(8)	−0.72(7)	1^-	1.64(21)	0.960(64)	1.75(32)		10.2(13)	
7863.5(6)	0.72(8)	1^+	1.42(25)	0.435(27)				0.76(14)
7896.0(6)	−0.79(6)	1^-	4.2(5)	3.38(17)	5.68(80)		24.3(17)	
8013.7(11)	0.70(9)	1^+	0.18(3)	0.260(59)				0.091(17)
8090.5(6)	−0.74(6)	1^-	0.64(7)	0.734(44)	1.60(35)		3.4(4)	
8175.0(7)	−0.76(11)	1^-	0.15(3)	0.23(5)			2.7(5)	
8764(1)	−0.77(6)	1^-	0.56(6)	0.441(37)			2.4(3)	
8956.3(10)	−0.76(7)	1^-	0.36(4)	0.233(36)			1.5(2)	
9139.4(5)	0.84(5)	1^+	2.39(27)	2.65(15)	2.93(51)	2.68(16)		0.81(18)
9211.0(5)	0.78(5)	1^+	2.38(25)$^{\mathrm{f}}$	2.11(14)	2.76(59)			0.79(8)
9236.1(6)	−0.75(6)	1^-	0.38(4)	0.503(55)			1.4(1)	
9327.1(6)	0.63(5)	1^+	0.44(5)	0.746(80)				0.14(2)
9427.4(7)	0.86(6)	1^+	0.28(4)	0.95(11)				0.087(11)
9735.6(7)	0.81(6)	$(1)^+$	0.96(11)					0.27(3)
9787.4(6)	−0.84(5)	1^-	1.66(16)		4.01(61)		5.1(5)	
9982.0(6)	−0.78(5)	$(1)^-$	0.61(6)				1.8(2)	
10434.8(9)	−0.37(20)	$(1)^-$	0.96(24)				2.4(6)	
10929.1(8)	−0.91(6)	$(1)^-$	0.92(10)				2.0(2)	
11769(2)	−0.80(6)	$(1)^-$	2.92(29)				5.1(5)	
11836(2)	−0.81(6)	$(1)^-$	1.40(15)				2.42(26)	

$^{\mathrm{a}}$This work. The statistical and systematic uncertainties associated with strength normalization (4%), photon flux (5%), and efficiency (5%) are reflected in the errors.
$^{\mathrm{b}}$Values taken from Refs. [29,30].
$^{\mathrm{c}}$Values taken from Ref. [25].
$^{\mathrm{d}}$Values taken from Ref. [27].
$^{\mathrm{e}}$$\Gamma_0/\Gamma = 1$ is assumed except for the 8175-keV state, for which $\Gamma_0/\Gamma = 0.28(4)$ is obtained from the present measurement.
$^{\mathrm{f}}$Contribution from ^{50} is subtracted.

TABLE II. Possible transitions in ^{52}Cr. Transition energies E_γ, intensity asymmetry A, spin and parity assignments J^π, scattering strengths Γ_0^2/Γ, and reduced transition probabilities $B(\sigma 1)\uparrow$ are listed.

E_γ (keV)	A	J^π	Γ_0^2/Γ[a] (eV)	$B(E1)\uparrow$[b] (10^{-3} e^2 fm^2)	$B(M1)\uparrow$[b] (μ_N^2)
7819(1)	$-0.36(32)$	(1^-)	0.16(6)	0.93(33)	
7947(2)	0.68(25)	$(1,2)^+$	0.06(5)[c,d]		0.031(28)[d]
7957(2)	$-0.60(25)$	$(1)^-$	0.07(4)	0.38(21)	
8112.8(13)	$-0.67(19)$	$(1)^-$	0.05(2)	0.25(10)	
8214(2)	$-0.76(14)$	$(1)^-$	0.05(2)	0.27(12)	
8356.1(11)	$-0.35(32)$	(1^-)	0.10(5)	0.47(27)	
8402.3(8)	0.81(10)	$(1)^+$	0.28(5)		0.12(2)
8583.2(9)	0.74(8)	$(1)^+$	0.28(4)		0.12(2)
9025.9(13)	$-0.22(21)$	$(1)^-$	0.16(3)	0.64(13)	
9061.3(7)	0.55(26)	$(1)^+$	0.11(4)		0.038(14)
9112.9(11)	$-0.79(10)$	$(1)^-$	0.12(2)	0.47(7)	
9159.3(11)	$-0.70(10)$	$(1)^-$	0.18(2)	0.66(9)	
9284.0(11)	$-0.52(18)$	$(1)^-$	0.06(1)	0.22(5)	
9369(2)	$-0.42(36)$	(1^-)	0.02(1)	0.075(29)	
9621.8(9)	0.75(6)	$(1)^+$	0.50(7)		0.15(2)
9637.7(11)	$-0.71(22)$	$(1)^-$	0.27(10)	0.85(31)	
9719.4(9)	$-0.86(6)$	$(1)^-$	0.47(5)	1.5(2)	
9720.9(11)	0.51(24)	(1^+)	0.28(10)[c]		0.079(29)
9841.5(9)	0.83(5)	$(1)^+$	0.43(5)		0.12(1)
9890.9(7)	0.85(6)	$(1)^+$	0.43(5)		0.11(1)
9983.6(12)	0.79(6)	$(1,2)^+$	0.24(3)[d]		0.063(8)[d]
10007.9(8)	0.71(7)	(1^+)	0.14(2)		0.036(5)
10010.3(11)	$-0.81(10)$	$(1)^-$	0.094(13)	0.27(4)	
10037.9(12)	$-0.81(7)$	$(1)^-$	0.13(2)	0.38(5)	
10068.7(9)	$-0.54(30)$	$(1)^-$	0.03(1)	0.10(4)	
10194.5(9)	0.60(22)	$(1,2)^+$	2.1(5)[d]		0.51(13)[d]
10352.0(9)	0.60(23)	$(1)^+$	0.92(26)		0.22(6)
10566.4(13)	$-0.71(18)$	$(1)^-$	0.21(11)	0.51(26)	
10576.5(11)	0.50(16)	$(1,2^+)$	0.84(17)[d]		0.19(4)[d]
10804.8(14)	0.79(7)	$(1)^+$	0.55(8)		0.11(2)
10927.0(12)	0.78(7)	$(1)^+$	0.26(4)		0.051(8)
10998.3(10)	$-0.82(7)$	$(1)^-$	0.61(10)	1.3(2)	
11337(2)	0.58(26)	$(1)^+$	1.2(3)		0.21(6)
11367(2)	$-0.59(12)$	(1^-)	1.6(3)	3.2(6)	
11384(2)	$-0.43(16)$	(1^-)	0.96(23)	1.9(4)	
11410(2)	0.74(6)	$(1)^+$	3.4(7)		0.60(12)
11800(2)	0.40(40)	$(1)^+$	0.18(8)		0.028(12)
11868(2)	$-0.77(11)$	$(1)^-$	0.34(6)	0.58(11)	
11953(2)	$-0.75(9)$	$(1)^-$	0.32(6)	0.54(10)	
12062(2)	$-0.77(7)$	$(1)^-$	0.71(8)	1.2(1)	
12079(2)	$-0.77(8)$	$(1)^-$	0.52(8)	0.84(12)	

[a]The statistical and systematic uncertainties associated with strength normalization (4%), photon flux (5%), and efficiency (5%) are reflected in the errors.

[b]$\Gamma_0/\Gamma = 1$ is assumed.

[c]Contribution from ^{50}Cr is subtracted.

[d]Assumed as $M1$ transitions.

the resonances listed in Table II are included, $\Sigma B(M1)\uparrow = 7.03(38)$ μ_N^2; the summed $E1$ strength is $\Sigma B(E1)\uparrow = 64.7(24) \times 10^{-3}$ e^2 fm^2, or if the resonances listed in Table II are included, $\Sigma B(E1)\uparrow = 82.3(27) \times 10^{-3}$ e^2 fm^2. The $M1$ and $E1$ strengths at $E_x = 5.0$ to 7.5 MeV are known to be $\Sigma B(M1)\uparrow = 0.20(2)$ μ_N^2 and $\Sigma B(E1)\uparrow = 9.4(4) \times 10^{-3}$ e^2 fm^2, respectively [29,30]. By adding these values to the

present results, the summed $M1$ and $E1$ strengths are $\Sigma B(M1)\uparrow = 7.24(38)$ μ_N^2 and $\Sigma B(E1)\uparrow = 91.7(27) \times 10^{-3}$ e^2 fm^2, respectively at $E_x = 5.0$ to 12.1 MeV. In a previous inelastic electron scattering measurement [5], the weighted sum $M1$ strength of 7.47(47) μ_N^2 in the excitation energy range from 7 to 12 MeV was obtained. The present summed $M1$ strength is in good agreement with this value. Furthermore, the

present summed $E1$ strength corresponds to 0.43(1)% of the energy-weighted TRK sum rule value, which is consistent with the values measured for ^{56}Fe and ^{58}Ni [20,21]. In the present analysis, we found that the relaxation of the significance limit for the identification of peaks from 3σ to 2σ led to about 10% more strength. This strongly indicates that more strength is likely hidden in the background.

IV. DISCUSSION

In this section, the measured $M1$ and $E1$ strength distributions of ^{52}Cr are compared with theoretical predictions based on RPA and second RPA (SRPA) calculations. The former includes only one-particle–one-hole (1p1h) excitations, whereas the latter takes into account 2p2h excitations in addition to the 1p1h excitations.

In the present calculation, a self-consistent Hartree-Fock (SHF) method was used in the coordinate space with a box size $r = 20$ fm with a step of $\Delta r = 0.1$ fm to calculate single-particle states. We chose the SGII interaction [38] as the effective center and spin-orbit forces, and the Te1 interaction as the tensor force [39]. The equal filling approximation was applied to describe the open-shell structure for ^{52}Cr. Namely, the occupation probabilities were set as $n = 1$ for the proton $1s$, $1p$, $1d$, and $2s$ states and $n = 0.5$ for the $1f_{7/2}$ state.

The single-particle levels (SPLs) obtained via the calculations using the SGII and SGII+Te1 interactions are shown in Fig. 5. The proton SPLs are less sensitive to the tensor force than the neutron SPLs. Whereas the neutron $1f_{7/2}$ state outside the $N = 20$ LS(spin-orbit)-closure core is fully occupied, the proton $1f_{7/2}$ state is half-filled. Thus, more strongly influences on the neutron LS potential are expected. The additional LS potential invoked by the tensor force is given by

$$\Delta U_q = \alpha_T \frac{J_q}{r} + \beta_T \frac{J_{q'}}{r}, \qquad (7)$$

where q and q' represent the proton and neutron, respectively, or neutron and proton. The tensor force parameters α_T and β_T are -145.7 and 31.3 fm^{-3} MeV, respectively. If we approximate $2J_p = J_n = J > 0$, we obtained $r\Delta U_n = J(\alpha_T + \beta_T/2)$ and $r\Delta U_p = J(\alpha_T/2 + \beta_T)$. Consequently, ΔU_n is larger than ΔU_p. The LS gaps between the $1f_{5/2}$ and $1f_{7/2}$ states for the neutron and proton orbits become larger for the SGII+Te1 interaction, which affects the $M1$ strength distribution as shown below.

To perform the RPA and SRPA calculations, the continuum states are discretized by the box used in the SHF calculation. The SPLs with energies of up to 30 MeV are taken into account. The cutoff energies of unperturbed 1p1h and 2p2h states are fixed at 100 MeV. The $M1$ transition operators for isoscalar and isovector are given by

$$\mathcal{O}_{M1,\mathrm{is}} = \sqrt{\frac{3}{4\pi}} \mu_N \sum_i \frac{1}{2} g_l(i)\vec{l}_i + \frac{1}{2}\left(g_s^p + g_s^n\right)\vec{s}_i,$$

$$\mathcal{O}_{M1,\mathrm{iv}} = \sqrt{\frac{3}{4\pi}} \mu_N \sum_i g_l(i)\vec{l}_i + \left(g_s^p - g_s^n\right)\vec{s}_i \tau_z(i), \quad (8)$$
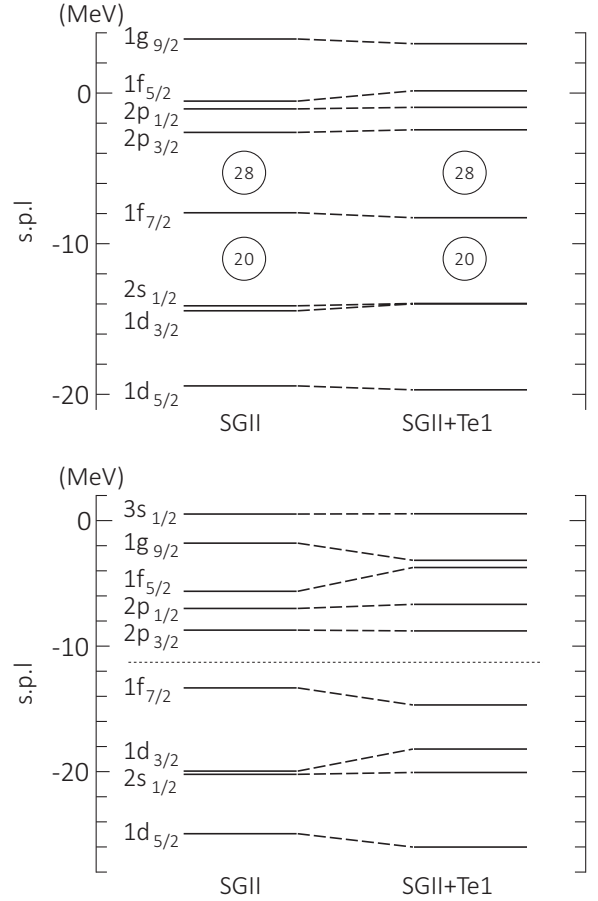

FIG. 5. SPLs of protons (top) and neutrons (bottom) for ^{52}Cr calculated with the SGII and SGII+Te1 interactions. The dotted line in the right panel indicates the Fermi energy of the neutrons.

where $g_s^p = 5.58\zeta_p$ and $g_s^n = -3.82\zeta_n$. In the present calculation, quenching factors of $\zeta_p = \zeta_n = 0.8$ are used. These values agree with the average value from Refs. [40] and [41]. The same values are also used in the $M1$ strength calculations based on the Monte Carlo shell model [42] and the quasiparticle phonon model (QPM) [30]. The $E1$ transition operator is given by

$$\mathcal{O}_{E1} = e^2 \sum_{i \in p} [r_i Y_{10}(\hat{r}_i) - R Y_{10}(\hat{r})]. \qquad (9)$$

The $M1$ and $E1$ reduced transition probabilities can be calculated using the RPA and SRPA coefficients,

$$
\begin{aligned}
B(\sigma 1) &= |\langle \nu | \mathcal{O}_{\sigma 1} | 0 \rangle|^2 \\
&\approx \sum_{ph} |\langle p || \mathcal{O}_{\sigma 1} || h \rangle (X_{ph} - Y_{ph})|^2 (n_h - n_p), \quad (10)
\end{aligned}
$$

where the index $\sigma 1$ denotes $M1$ or $E1$. The present RPA and SRPA calculations were performed within the framework of Ref. [31], in which Gamow-Teller transitions were investigated using the 2p2h Tamm-Dancoff approximation. It has been noted that the use of δ interaction like the Skyrme force causes the so-called ultraviolet divergence [43] in particle-particle matrix elements in the residual interaction of SRPA. This
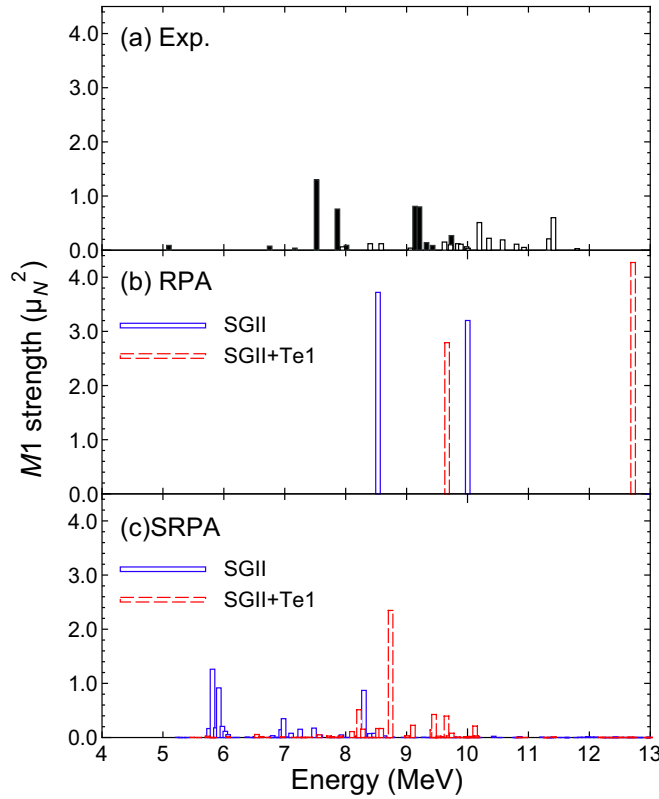
FIG. 6. Distribution of (a) the measured $E1$ strength in units of μ_N^2 in ^{52}Cr compared with the values obtained from (b) RPA and (c) SRPA calculations with the SGII and SGII+Te1 interactions. Experimental data listed in Table I (Table II) are shown with black (white) bars. In addition, experimental data below 7.5 MeV are taken from Refs. [29,30].

problem is frequently discussed when the δ interaction is used for a correlation due to particle-particle interaction and already appears in Hartree-Fock-BCS and Hartree-Fock-Bogoliubov [44]. There is also a double-counting problem [45], which requires readjustment of the parameters used in the effective interaction. One way to avoid this problem is to use the subtracted method [45,46]. In this work, to minimize undesirable correlations arising from the ultraviolet divergence and double counting problem, a restricted SPL space is used, as done in Refs. [31,46]. This prescription has shown to provide
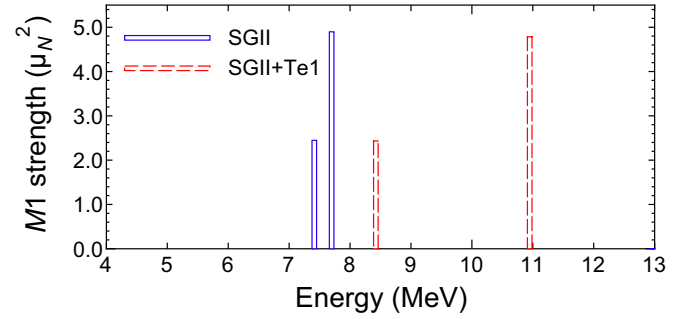

FIG. 7. Calculated $M1$ strength in units of μ_N^2 obtained for the unperturbed states.

a reasonable result in terms of the 2p2h configuration mixing effect. SPLs in the vicinity of the Fermi energy, that is, $2s_{1/2}$, $1d_{3/2}$, $1f_{5/2}$, $1f_{7/2}$, $2p_{1/2}$, $2p_{3/2}$, and $1g_{9/2}$ neutron orbits and $1d_{3/2}$, $2s_{1/2}$, $1f_{5/2}$, $1f_{7/2}$, $2p_{1/2}$, and $2p_{3/2}$ proton orbits were considered to form unperturbed 2p2h states. In the SRPA calculation for the open shell nucleus, we used the partial occupation numbers given in Eq. (8) of Ref. [47].

We compare the measured $M1$ strength of ^{52}Cr with the predicted $M1$ strength obtained in the RPA and SRPA calculations in Fig. 6. The RPA calculation with the SGII interaction generates two peaks at approximately 8.5 and 10.0 MeV with strengths of 3.0 and 3.5 μ_N^2. By contrast, the observed $M1$ resonances are widely distributed from 7 to 12 MeV and have the maximum strength of approximately 1 μ_N^2. The RPA calculation with the SGII+Te1 interaction also gives two strong peaks at higher energies than the SGII interaction. This result occurs because the tensor force increases the energy gap between the $1f_{7/2}$ and $1f_{5/2}$ orbits, as mentioned above. This effect can be clearly observed in Fig. 7, which presents the results obtained in the $M1$ strength calculation for the unperturbed states equivalent to those for the single-particle transition. The lower (higher) peak corresponds to the transition of proton (neutron) states from $1f_{7/2}$ to $1f_{5/2}$. The peak positions for the SGII+Te1 interaction are higher than those for the SGII interaction because a larger energy gap exists between the $1f_{7/2}$ and $1f_{5/2}$ orbits as a result of the tensor force. The total $M1$ strengths at excitation energies of up to 13 MeV obtained in the RPA calculation are 6.9 and 7.1 μ_N^2 for the SGII and SGII+Te1 interaction, respectively.

TABLE III. Particle-hole configuration and amplitude ($X^2 - Y^2$) contributing to the lower and higher energy resonances, obtained in the RPA calculations with the SGII and SGII+Te1 interactions.

	Lower resonance			Higher resonance	
Configuration	SGII 8.5 MeV	SGII+Te1 9.7 MeV	Configuration	SGII 10.0 MeV	SGII+Te1 12.7 MeV
$\pi\{1f_{5/2}, 1f_{7/2}^{-1}\}$	96.4%	98.8%	$\nu\{1f_{5/2}, 1f_{7/2}^{-1}\}$	96.0%	95.6%
$\pi\{1f_{5/2}, 1p_{3/2}^{-1}\}$	0%	0.2%	$\nu\{1f_{5/2}, 1p_{3/2}^{-1}\}$	0%	0.8%
$\pi\{3g_{7/2}, 1d_{5/2}^{-1}\}$	0%	0.2%	$\nu\{3g_{7/2}, 1d_{5/2}^{-1}\}$	0%	0.5%
$\nu\{1f_{5/2}, 1f_{7/2}^{-1}\}$	3.5%	0.2%	$\pi\{1f_{5/2}, 1f_{7/2}^{-1}\}$	3.5%	0.2%

In Table III, the particle-hole configuration and amplitude contributing to the lower and higher energy resonances obtained in the RPA calculations are listed. The configuration of the lower energy resonance calculated with the SGII inter-action is $\pi\{1f_{5/2}, 1f_{7/2}^{-1}\}$ (96.4%)[1] and $\nu\{1f_{5/2}, 1f_{7/2}^{-1}\}$ (3.5%), whereas that of the higher energy resonance is $\nu\{1f_{5/2}, 1f_{7/2}^{-1}\}$ (96.0%) and $\pi\{1f_{5/2}, 1f_{7/2}^{-1}\}$ (3.5%). By contrast, the con-figuration of the lower energy resonance calculated with the SGII+Te1 interaction consists of $\pi\{1f_{5/2}, 1f_{7/2}^{-1}\}$ (98.8%) and other particle-hole configurations, such as $\pi\{1f_{5/2}, 1p_{3/2}^{-1}\}$ (0.2%), $\pi\{3g_{7/2}, 1d_{5/2}^{-1}\}$ (0.2%), and $\nu\{1f_{5/2}, 1f_{7/2}^{-1}\}$ (0.2%). The first two configurations have $\Delta L = 2$, where L is the orbital angular momentum. These particle-hole configura-tions are a typical consequence of the inclusion of the tensor force. The lower resonance is mainly produced by proton configurations. A neutron particle-hole configuration of $\nu\{1f_{5/2}, 1f_{7/2}^{-1}\}$ also contributes to the resonance with a small amplitude 3.5%. However, it decreases to 0.2% in case of SGII+Te1, namely the isovector nature is weakened by the tensor force. This behavior could be attributed to the increased energy gap between the $1f_{7/2}$ and $1f_{5/2}$ orbits and the enlargement of the two-body collision channels by the tensor force enhancing $\Delta L = 2$ particle-hole configurations. A similar result is obtained in the higher energy resonance, which is dominated by $\nu\{1f_{5/2}, 1f_{7/2}^{-1}\}$ (95.6%) with other many configurations, such as $\nu\{1f_{5/2}, 1p_{3/2}^{-1}\}$ (0.8%), $\nu\{3g_{7/2}, 1d_{5/2}^{-1}\}$ (0.5%), and $\pi\{1f_{5/2}, 1f_{7/2}^{-1}\}$ (0.2%). Similar to the lower energy resonance, the tensor force decreases the proton particle-hole configuration mixing from 3.5% to 0.2%, reducing the isovector nature.

The $M1$ strength obtained in the SRPA calculations shown in the bottom panel of Fig. 6 exhibits a wide distribution unlike that obtained in the RPA calculations. This result is a consequence of 2p2h configuration mixing. The configuration of the resonance at 8.3 MeV for the SRPA calculation with the SGII interaction is dominated by $\pi\{1f_{5/2}, 1f_{7/2}^{-1}\}$ (52.1%) and approximately 47% arises from the 2p2h configurations. The calculated resonance energies are lower than the observed values. Including the tensor force shifts the calculated peak positions to higher energies, as shown for the RPA calculations. The configuration of the resonance at 8.7 MeV is dominated by $\nu\{1f_{5/2}, 1f_{7/2}^{-1}\}$ (34.8%) and approximately 62% arises from the 2p2h configurations. The total $M1$ strengths at excitation energies of up to 12 MeV obtained in the SRPA calculation are 5.2 and 5.4 μ_N^2 for the SGII and SGII+Te1 interactions, respectively.

In a previous study, QPM was used to calculate 1^+ excited states in ^{52}Cr by including one-, two-, and three-phonon configurations with J^π ranging from $1^\pm$ to $6^\pm$ at excitation energies of up to 9.8 MeV [30]. The $M1$ strength in the energy region from 5.1 to 9.5 MeV was calculated to be 3.1 μ_N^2. This value is smaller than the value of 4.5μ_N^2 in the same energy region obtained by the present SRPA calculations

with the SGII+Te1 interaction. The previous QPM calculation also indicated strong fragmentation of the $M1$ strength at higher energies over a considerable number of 1^+ states with relatively low transition probabilities and a summed $M1$
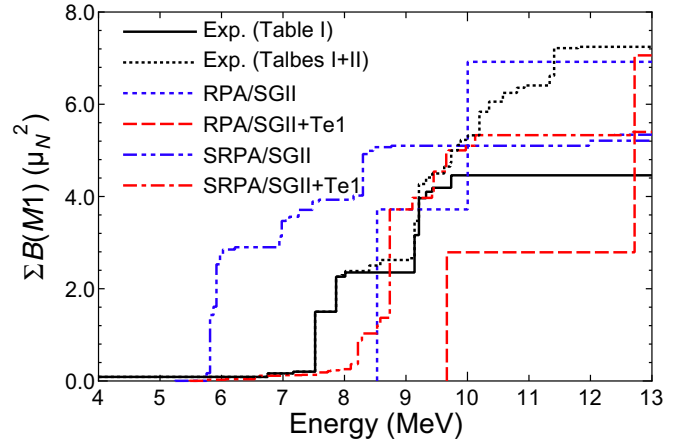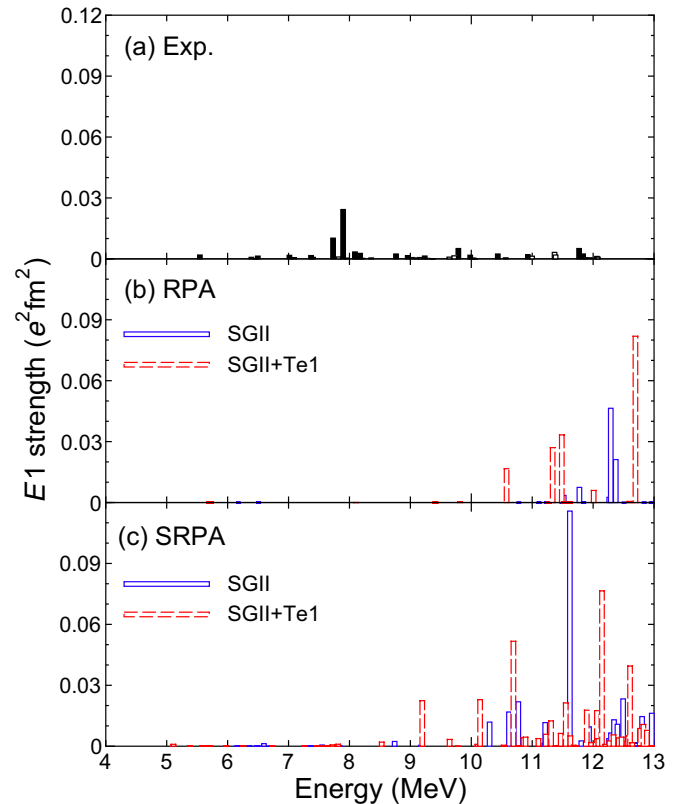

FIG. 8. Comparison of the measured and calculated RPA and SRPA cumulative $M1$ strengths. The experimental values from Table I (Tables I and II) are shown with solid (dotted) lines. Experimental $B(M1)$ data below 7.5 MeV are taken from Refs. [29,30].

FIG. 9. Distribution of (a) the measured $E1$ strength in units of e^2 fm^2 in ^{52}Cr compared with the values obtained from (b) RPA and (c) SRPA calculations with the SGII and SGII+Te1 interactions. Experimental data listed in Table I (Table II) are shown with black (white) bars. In addition, experimental data below 7.5 MeV are taken from Refs. [29,30].

----

[1]The number in percentage following particle-hole configuration is the RPA amplitude calculated by $X_{ph}^2 - Y_{ph}^2$.
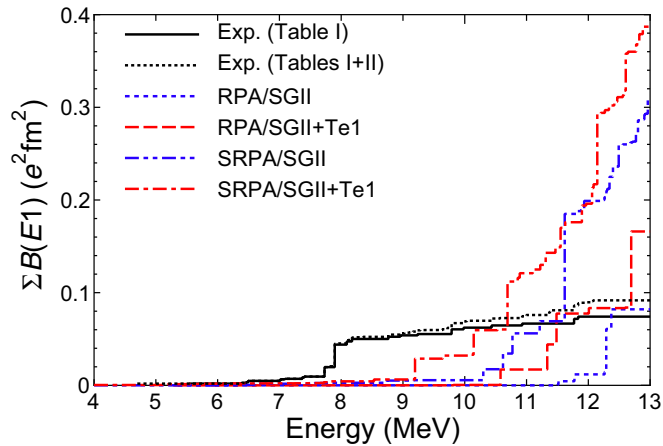
FIG. 10. Comparison of the measured and calculated RPA and SRPA cumulative $E1$ strength. The experimental values from Table I (Tables I and II) are shown with solid (dotted) lines. Experimental $B(E1)$ data below 7.5 MeV are taken from Refs. [29,30].

strength of approximately 6 μ_N^2 in the excitation energy range from 10 to 12.5 MeV. In the present work, $M1$ strength of approximately 2 μ_N^2 was obtained at $E_x = 10$ to 12 MeV. However, it should be noted that the $M1$ strength measured here does not include the contributions of branching to excited states and of weak peaks hidden in the background, which could increase the $M1$ strength.

To demonstrate the impact of the effects of 2p2h configuration mixing and the tensor force, we show the cumulative $M1$ strength as a function of the excitation energy in Fig. 8. The results from the RPA calculations with the SGII and SGII+Te1 interactions indicate simple two-step increments. By contrast, the results from the SRPA calculations reveal a more complicated structure because of 2p2h configuration mixing. The SRPA calculation with the SGII+Te1 interaction reproduces the gross structure of the experimental data.

Based on the present measurements, the summed $E1$ strength at excitation energies from 5.0 to 12.1 MeV in ^{52}Cr was determined as $\Sigma B(E1)\uparrow = 83.1(23) \times 10^{-3}$ e^2 fm^2. Almost half of this $E1$ strength is associated with two transitions at 7730.3 and 7896.0 keV, which form a small $E1$ concentration below the neutron separation energy. In a previous study using QPM [30], the 1^- state with the strongest $E1$ transition probability below 9.8 MeV contained contributions from the low-energy tail of the GDR.

Figure 9 demonstrates the results of the $E1$ strength calculations using the RPA and SRPA. The RPA calculation predicts little $E1$ strength around $E_x = 8$ MeV, whereas the SRPA calculation predicts an $E1$ strength of 3×10^{-3} to 4×10^{-3} e^2 fm^2, which is more than 10 times smaller than the measured value. The configuration obtained via the SRPA calculations is dominated by 1p1h configurations such as $\nu\{2p_{3/2}, 1d_{3/2}^{-1}\}$, $\nu\{1g_{9/2}, 1f_{7/2}^{-1}\}$, $\pi\{2p_{3/2}, 1d_{3/2}^{-1}\}$, and many 2p2h configurations. No obvious enhancement of the $E1$ strength below 9 MeV was observed in the present calculations.

As shown in Fig. 10, the dependence of the cumulative $E1$ strength on the excitation energy is not well reproduced. Including 2p2h configuration mixing and the tensor force in the SRPA calculation shifts the excitation energies of the 1^- states to lower energy, which is closer to the experimental result. However, the cumulative $E1$ strength at 12 MeV is more than twice the measured value. The SRPA calculation also indicates a significant increase of the $E1$ strength above 12 MeV where the GDR strength becomes dominant.

V. CONCLUSION

In conclusion, NRF experiments on ^{52}Cr were conducted using a quasimonochromatic, linearly polarized photon beam. A total of 62 states were observed in the energy region from 7.5 to 12.1 MeV. The parities were determined based on the intensity asymmetry of scattered γ rays with respect to the polarization plane of the incident photon beam. The observed $M1$ and $E1$ strengths of ^{52}Cr were compared with the results of the RPA and SRPA calculations. The RPA calculation fails to reproduce the fragmentation pattern of the $M1$ strength. When 2p2h configuration mixing was included in the SRPA calculation, the $M1$ strength become widely distributed, giving results consistent with the experimental data. The tensor force tends to increase the resonance energy, which is important for reproducing the gross structure of the measured cumulative $M1$ strength. The $E1$ strength was also investigated using the RPA and SRPA calculations. Although the experimental data were not well reproduced, 2p2h configuration mixing and the tensor force reduced the discrepancy between the measured and predicted excitation energies of the 1^- states.

[1] K. Heyde, P. von Neumann–Cosel, and A. Richter, Rev. Mod. Phys. **82**, 2365 (2010).

[2] D. Savran, T. Aumann, and A. Zilges, Prog. Part. Nucl. Phys. **70**, 210 (2013).

[3] A. Bohr and B. R. Mottelson, *Nuclear Structure* (Benjamin, New York, 1975).

[4] G. Eulenberg, D. I. Sober, W. Steffen, H.-D. Gräf, G. Küchler, A. Richter, E. Spamer, B. C. Metsch, and W. Knüpper, Phys. Lett. B **116**, 113 (1982).

[5] D. I. Sober, B. C. Metsch, W. Knüpfer, G. Eulenberg, G. Küchler, A. Richter, E. Spamer, and W. Steffen, Phys. Rev. C **31**, 2054 (1985).

[6] W. Mettner, A. Richter, W. Stock, B. C. Metsch, and A. G. M. van Hees, Nucl. Phys. A **473**, 160 (1987).

[7] R. W. Fearick, G. Hartung, K. Langanke, G. Martínez-Pinedo, P. von Neumann–Cosel, and A. Richter, Nucl. Phys. A **727**, 41 (2003).

[8] J. Speth, V. Klemt, J. Wambach, and G. E. Brown, Nucl. Phys. A **343**, 382 (1980).

[9] J. Wambach, A. D. Jackson, and J. Speth, Nucl. Phys. A **348**, 221 (1980).

[10] D. Cha, B. Schwesinger, J. Wambach, and J. Speth, Nucl. Phys. A **430**, 321 (1984).

[11] T. Hartmann, M. Babilon, S. Kamerdzhiev, E. Litvinova, D. Savran, S. Volz, and A. Zilges, Phys. Rev. Lett. **93**, 192501 (2004).

[12] P. Adrich, A. Klimkiewicz, M. Fallot, K. Boretzky, T. Aumann, D. Cortina-Gil, U. Datta Pramanik, T. W. Elze, H. Emling, H. Geissel *et al.*, Phys. Rev. Lett. **95**, 132501 (2005).

[13] O. Wieland, A. Bracco, F. Camera, G. Benzoni, N. Blasi, S. Brambilla, F. C. L. Crespi, S. Leoni, B. Million, R. Nicolini *et al.*, Phys. Rev. Lett. **102**, 092502 (2009).

[14] D. Savran, M. Fritzsche, J. Hasper, K. Lindenberg, S. Müller, V. Yu. Ponomarev, K. Sonnabend, and A. Zilges, Phys. Rev. Lett. **100**, 232501 (2008).

[15] A. P. Tonchev, S. L. Hammond, J. H. Kelley, E. Kwan, H. Lenske, G. Rusev, W. Tornow, and N. Tsoneva, Phys. Rev. Lett. **104**, 072501 (2010).

[16] A. Leistenschneider, T. Aumann, K. Boretzky, D. Cortina, J. Cub, U. Datta Pramanik, W. Dostal, T. W. Elze, H. Emling, H. Geissel *et al.*, Phys. Rev. Lett. **86**, 5442 (2001).

[17] N. Ryezayeva, T. Hartmann, Y. Kalmykov, H. Lenske, P. von Neumann–Cosel, V. Yu. Ponomarev, A. Richter, A. Shevchenko, S. Volz, and J. Wambach, Phys. Rev. Lett. **89**, 272502 (2002).

[18] J. Piekarewicz, Phys. Rev. C **73**, 044325 (2006).

[19] B. A. Brown, Phys. Rev. Lett. **85**, 5296 (2000).

[20] F. Bauwens, J. Bryssinck, D. De Frenne, K. Govaert, L. Govor, M. Hagemann, J. Heyse, E. Jacobs, W. Mondelaers, and V. Y. Ponomarev, Phys. Rev. C **62**, 024302 (2000).

[21] T. Shizuma, T. Hayakawa, H. Ohgaki, H. Toyokawa, T. Komatsubara, N. Kikuzawa, T. Inakura, M. Honma, and H. Nakada, Phys. Rev. C **87**, 024301 (2013).

[22] U. Kneissl, H. H. Pitz, and A. Zilges, Prog. Part. Nucl. Phys. **37**, 349 (1996).

[23] N. Pietralla, Z. Berant, V. N. Litvinenko, S. Hartman, F. F. Mikhailov, I. V. Pinayev, G. Swift, M. W. Ahmed, J. H. Kelley, S. O. Nelson *et al.*, Phys. Rev. Lett. **88**, 012502 (2001).

[24] T. Shizuma, T. Hayakawa, H. Ohgaki, H. Toyokawa, T. Komatsubara, N. Kikuzawa, A. Tamii, and H. Nakada, Phys. Rev. C **78**, 061303(R) (2008).

[25] N. Kumagai, T. Ishimatsu, E. Tanaka, K. Kageyama, and G. Isoyama, Nucl. Phys. A **329**, 205 (1979).

[26] U. E. P. Berg, D. Rück, K. Ackermann, K. Bangert, C. Bläsing, K. Kobras, W. Naatz, R. K. M. Schneider, R. Stock, and K. Wienhard, Phys. Lett. B **103**, 301 (1981).

[27] P. B. Smith and W. Segeth, Nucl. Phys. A **398**, 397 (1983).

[28] J. Enders, P. von Brentano, J. Eberth, R.-D. Herzberg, N. Huxel, H. Lenske, P. von Neumann–Cosel, N. Nicolay, N. Pietralla, H. Prade *et al.*, Nucl. Phys. A **636**, 139 (1998).

[29] H. Pai, J. Beller, N. Benouaret, J. Enders, T. Hartmann, O. Karg, P. von Neumann–Cosel, N. Pietralla, V. Y. Ponomarev, C. Romig *et al.*, Phys. Rev. C **88**, 054316 (2013).

[30] Krishichayan, M. Bhike, W. Tornow, G. Rusev, A. P. Tonchev, and N. Tsoneva, and H. Lenske, Phys. Rev. C **91**, 044328 (2015).

[31] F. Minato, Phys. Rev. C **93**, 044319 (2016).

[32] S. Miyamoto, Y. Asano, S. Amano, D. Li, K. Imasaki, H. Kinugasa, Y. Shoji, T. Takagi, and T. Mochizuki, Radiat. Meas. **41**, S179 (2006).

[33] S. Amano, K. Horikawa, K. Ishihara, S. Miyamoto, T. Hayakawa, T. Shizuma, and T. Mochizuki, Nucl. Instrum. Methods Phys. Res. Sect. A **602**, 337 (2009).

[34] H. Hirayama, Y. Namito, A. F. Bielajew, S. J. Wilderman, and W. R. Nelson, The EGS5 code systems, SLAC Report 730, 2010, High Energy Accelerator Research Organization, Tsukuba.

[35] L. W. Fagg and S. S. Hanna, Rev. Mod. Phys. **31**, 711 (1959).

[36] F. Metzger, in *Progress in Nuclear Physics*, edited by O. Frisch (Pergamon Press, New York, 1959), Vol. 7, pp. 53–88.

[37] H. Pai, T. Beck, J. Beller, R. Beyer, M. Bhike, V. Derya, U. Gayer, J. Isaak, Krishichayan, J. Kvasil *et al.*, Phys. Rev. C **93**, 014318 (2016).

[38] N. Van Giai and H. Sagawa, Phys. Lett. B **106**, 379 (1981).

[39] C. L. Bai, H. Q. Zhang, H. Sagawa, X. Z. Zhang, G. Coló, and F. R. Xu, Phys. Rev. C **83**, 054316 (2011).

[40] P. Vesely, J. Kvasil, V. O. Nesterenko, W. Kleinig, P.-G. Reinhard, and V. Yu. Ponomarev, Phys. Rev. C **80**, 031302(R) (2009).

[41] H. Sagawa, T. Suzuki, and M. Sasano, Phys. Rev. C **94**, 041303(R) (2016).

[42] S. E. Koonin, D. J. Dean, and K. Langanke, Annu. Rev. Nucl. Part. Sci. **47**, 463 (1997).

[43] K. Moghrabi, M. Grasso, X. Roca-Maza, and G. Colò, Phys. Rev. C **85**, 044323 (2012).

[44] W. Satuła, Phys. Scr. **T125**, 82 (2006); P. J. Borycki, J. Dobaczewski, W. Nazarewicz, and M. V. Stoitsov, Phys. Rev. C **73**, 044319 (2006).

[45] V. I. Tselyaev, Phys. Rev. C **75**, 024306 (2007).

[46] D. Gambacurta, M. Grasso, and J. Engel, Phys. Rev. C **92**, 034303 (2015).

[47] C. Yannouleas, Phys. Rev. C **35**, 1159 (1987).